The influence of condition of the monazite structured $La_{0.9}Y_{0.1}PO_4$ nanocrystals sintering on thermal and mechanical properties of the material

M. O. Enikeeva[1,2,*], O. V. Proskurina[1,2], E. S. Motaylo[2], D. P. Danilovich[2], V. V. Gusarov[1]

[1]Ioffe Institute, 26, Politekhnicheskaya St., 194021, St. Petersburg, Russia

[2]Saint Petersburg State Institute of Technology, 26, Moskovsky Ave., 190013, St. Petersburg, Russia

enikeevamo@gmail.com

A lanthanum orthophosphate- and yttrium-based monazite structured $La_{0.9}Y_{0.1}PO_4$ nanocrystalline material was synthesized. The influence of the thermal treatment temperature on its thermal and mechanical properties has been determined. It was shown that the hydrothermal treatment of coprecipitated phosphates at 230 °C for 110 minutes yielded monazite structured nanoparticles with the crystallite size of about 16 nm. Nanopowder thermal treatment for 20 min in the annealing-quenching mode at 1000–1400 °C resulted in obtaining compact materials, the porosity of which varied from 52 to 27% with the grain growth from $\sim$20 to $\sim$100 nm. Active sintering occurred at temperatures above 1300 °C. Nanocrystalline materials obtained by heat treatment at 1200 °C with a grain size of $\sim$40 nm have a porosity of 42%, microhardness of $H_v(25$ °C$) = 4\pm0.5$ GPa, thermal conductivity $\lambda(25$ °C$) = 0.4$ W$\cdot$m$^{-1}\cdot$K^{-1}, and can be used as thermal insulation material.

Keywords: hydrothermal treatment, lanthanum and yttrium orthophosphates, thermal diffusivity, specific heat capacity, thermal conductivity.

Received: 25 November 2021

Revised: 6 December 2021

1. Introduction

Many modern functional materials are produced from complex oxide compounds, e.g. ferrites, tungstates, phosphates and others [1–5]. Various branches of modern industry require materials with thermal insulation and barrier properties [6–9]. In this regard, rare earth element (*RE*) orthophosphates with monazite and zircon type structures are promising [10–14]. Monazites structured *RE* orthophosphates have a high melting temperature ($T_m \sim$2173–2345 K) [15,16], low water solubility [17], high isomorphic capacity [18–21], resistance to aggressive media [22] and radiation damage [23–25]. The physicochemical properties of *RE* orthophosphates determine the great interest in the study of materials based on them. The mechanical and thermal properties influence the long-term stability, thermal insulation properties and integrity of ceramic products.

Functional materials are obtained on the basis of individual *RE* orthophosphates, solid solutions, including nanocrystalline ones [26–35]. *RE* orthophosphate nanoparticles are of scientific interest to researchers, both from the fundamental and from practical points of view. A thorough study of the mechanisms of formation and stability of *RE* orthophosphate phases will help broaden their potential application in modern technology. At present, the obtaining of monazite REPO$_4$ ($RE=$ La – Gd) based materials are aimed at producing composites for the radioactive waste form [21,36–39], thermal barrier coatings [11,12], and for the manufacture of luminescent materials [26,40].

Pre-ceramic powders synthesis is an important stage for obtaining functional materials. The hydrothermal treatment synthesis makes it possible to obtain monazite structured single-phase nanopowders without their subsequent thermal treatment [41–43]. Under hydrothermal conditions, the process of structural transformation of the rhabdophane structured La(Y)PO$_4 \cdot n$H$_2$O solid solutions into monazite structured La(Y)PO$_4$ solid solutions occurs at lower temperatures ($T \approx$180 °C) than during aerobic calcination ($T \geq$500 °C) [21,44,45]. Besides, hydrothermal conditions ensure the obtaining of nanocrystalline powders and their greater uniformity in size and composition.

In the literature sources, one can find studies on the obtaining of non-porous macrocrystalline materials based on phases with monazite- or zircon-type structures by high-temperature calcination of rhabdophane structured phases [20, 36, 38]. The obtaining of nanocrystalline powders under hydrothermal conditions and subsequent sintering of the pressed samples in the annealing-quenching mode make it possible to produce porous nanocrystalline materials. Porous ceramics based on monazite structured phases can be considered as a thermal insulating material, since it can potentially have low thermal conductivity.

Despite numerous papers on the synthesis and study of the properties of materials based on monazite structured phosphates [5,16,46–48], there are practically no studies concerning nature-like nanocrystalline single-phase materials with yttrium or other *RE* additives.

Due to the above reasons, it is urgent to study the effects that the sintering temperature of monazite structured $La_{0.9}Y_{0.1}PO_4$ nanocrystalline pre-ceramic powders have on the thermal and mechanical properties of nature-like nanomaterials obtained from them.

2. Experimental

Monazite structured $La_{0.9}Y_{0.1}PO_4$ polycrystalline pre-ceramic nanopowders were synthesized in two stages. At the first stage, a solution of ammonium dihydrogen phosphate $NH_4H_2PO_4$ was added to a solution of lanthanum nitrate hexahydrate $La(NO_3)_3 \cdot 6H_2O$ (puriss.) and yttrium nitrate hexahydrate $Y(NO_3)_3 \cdot 6H_2O$ (puriss.) with constant stirring. The ratio of the reagent solutions was selected to ensure the stoichiometry specified for the reaction products. The resulting suspension with pH=1 was stirred for 15 minutes and placed in a Teflon liner of a steel autoclave (at 0.7 autoclave capacity). The autoclave was heated to 230 °C inside the furnace at $\sim$10 MPa inside the autoclave. The autoclave was kept in the furnace for 110 minutes at this temperature. After heat treatment, the autoclave was taken out from the furnace and naturally cooled down to room temperature. The solid phase was separated from the solution by decantation and rinsed with distilled water. The powder was dried at 85 °C for 48 hours.

The powder was molded into cylindrical pellets with an average diameter of 15 mm and a thickness of about 1.5 mm by uniaxial dry pressing at 4 MPa.

Sample sintering was carried out in the annealing-quenching mode as follows: the pressed tablets were placed in a heated furnace in a platinum crucible: sample 1 at 1000 °C, sample 2 at 1100 °C, sample 3 at 1200 °C, sample 4 at 1300 °C, and sample 5 at 1400 °C for 20 min for all samples. Then the samples were taken out and cooled down to room temperature (25 °C).

The X-ray phase analysis of the samples employed powder diffractograms recorded on a Rigaku SmartLab 3 powder diffractometer ($Cu_{K\alpha}$ emission) in the 2θ=10–80° angle range with a step of 0.01° and a scanning rate of 0.8°/min. The monazite phase was identified using the PDF 2 database. The average crystallite sizes were determined using the SmartLab Studio II software from Rigaku for all the peaks, using the Halder-Wagner method and taking into account the instrumental broadening of the instrument. The same SmartLab Studio II software was used to plot a lognormal crystallite size distribution for the monazite 020 peak.

The elemental composition and morphological features of powders and sintered samples were determined using a Tescan Vega 3 SBH scanning electron microscope (Tescan, Czech Republic) with an x-act detector Oxford Instruments (Oxford Instruments, United Kingdom) attachment for the X-ray spectral microanalysis. Due to the overlapping of the energy lines of the yttrium $L\alpha$-series (1.922 keV) and the phosphorus $K\alpha$-series (2.013 keV), the analysis of the nanopowder composition was carried out in the range up to 20 keV in 4–5 different regions, and the resulting value was obtained by averaging the obtained data.

The samples microhardness was determined by a PMT-3 microhardness tester (LOMO, Russia) by pressing a tetrahedral diamond pyramid in (Vickers method) at a load of 200 g for 10 s. At least five measurements were done for each sample.

The thermal properties of the materials were determined by the laser flash method using the LFA 457 MicroFlash (Netzsch, Germany) in the 25–825 °C range.

The specific heat values of the monazite structured $La_{0.9}Y_{0.1}PO_4$-based materials (at 25–825 °C) were processed by the least squares method to obtain the coefficients a, b and c according to the Mayer-Kelly equation $C_p = a + bT + cT^{-2}$ [49].

3. Results and discussion

The elemental analysis of the powder obtained by hydrothermal treatment at 230 °C for 110 minutes showed that the (La+Y):P atomic ratio is 48:52 ($\pm$1-2%), and the La:Y atomic ratio is 9:1 ($\pm$1-2%), i.e., it can be considered as corresponding to the $La_{0.9}Y_{0.1}PO_4$ stoichiometry within the error of the method.

The X-ray diffraction data on the initial powder and cylindrical pellets sintered from it (samples 1–5) are shown in Fig. 1. All samples have a monazite structure (PDF 00-012-0283). The monazite phase unit cells in all the samples have practically the same parameters: a=6.8147$\pm$0.0025 Å, b=7.0416$\pm$0.0050 Å, c=6.4916$\pm$0.0050 Å, V=303.32 Å^3, and $\rho_{calc.}$=5.0104 g/cm^3.

Figure 2 shows the dependence of the average crystallite size of the $La_{0.9}Y_{0.1}PO_4$ solid solution on the ceramics sintering temperature. The average crystallite size of the $La_{0.9}Y_{0.1}PO_4$ phase after hydrothermal treatment is about 16 nm. When sintering samples in the 1000–1200 °C range for 20 minutes (samples 1, 2, and 3), the average crystallite size gradually increases to 40 nm. An increase in the sintering temperature to 1300–1400 °C (samples 4, 5) leads to a sharp increase in the crystallite size up to 100$\pm$10 nm. The observed dependence allows one to conclude that the process of sintering and grain growth activates in the 1200 °C$< T <$1300 °C range.
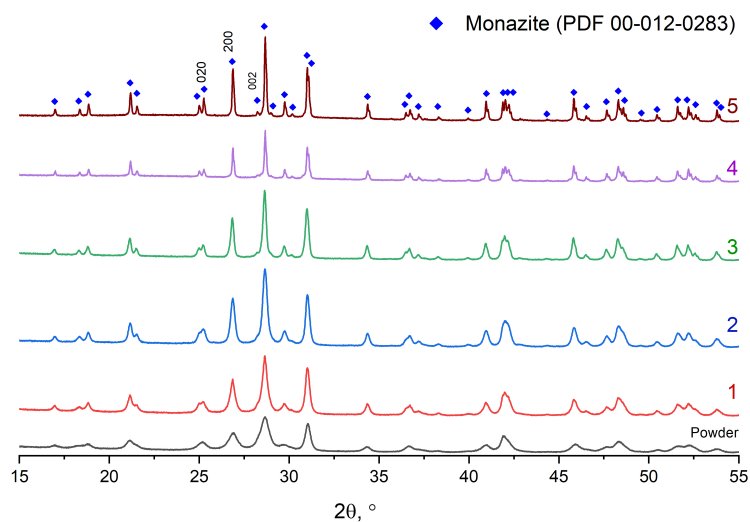
FIG. 1. X-ray diffraction patterns of the nanocrystalline powder (Powder) and samples after heat treatment at 1000 (1), 1100 (2), 1200 (3), 1300 (4), and 1400 °C (5)
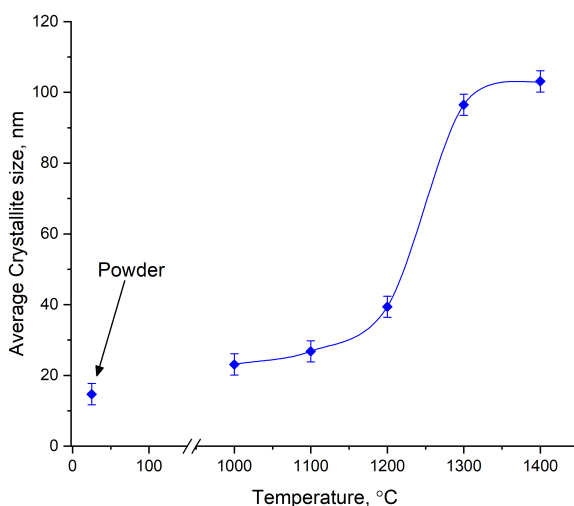

FIG. 2. Dependence of the average crystallite size on the sintering temperature

Figure 3 shows the crystallites size distribution for the initial powder and sintered samples, determined from the profile of the 020 peak of the monazite phase. It follows from the obtained data that crystallites of the initial powder have a narrow size distribution. The thermal treatments at 1000 °C and 1100 °C (samples 1 and 2) lead to an insignificant broadening of the distribution, while the heat treatment at 1200 °C (sample 3) broadens the size distribution of crystallites more noticeably, and the size distribution broadens significantly at 1300 °C and 1400 °C (samples 4 and 5).

Figure 4 demonstrates images of chips and polished sections of the samples sintered at 1000–1400 °C (specimens 1–5). The images of splinters (Fig. 4 a,c,e) and polished sections (Fig. 4 b,d,f) of samples 1–3 clearly show the fibrous microstructure of the samples formed by anisotropic nanoparticles of $La_{0.9}Y_{0.1}PO_4$ monazite. The images of splinter from samples 1 and 2 demonstrate a significant fraction of voids between the chaotically stacked monazite nanoparticle agglomerates. The topography of the polished sections from samples 1 and 2 (Fig. 4 b,d) has a similar appearance. Microstructural changes in the material begin at $T \approx 1200$ °C, the agglomerated fibers in its polished section (Fig. 4 f) are less pronounced than in the case of samples 1 and 2 (Fig. 4 b,d) obtained at lower temperatures.

The analysis of changes in the microstructure of materials after sintering, revealed by studies on a scanning electron microscope (SEM), and of the data on the crystallites growth during thermal treatment, allows a conclusion that
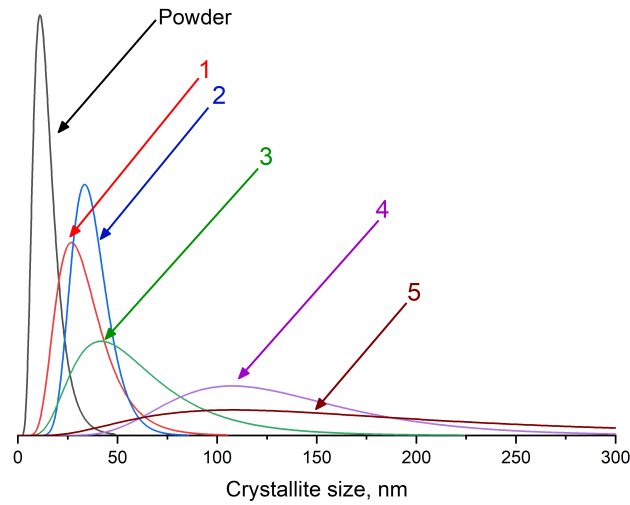
FIG. 3. Size distribution of crystallites of the initial powder (Powder) and samples after heat treatment at 1000 (1), 1100 (2), 1200 (3), 1300 (4), and 1400 °C (5)

TABLE 1. Characteristics of the $La_{0.9}Y_{0.1}PO_4$-based materials

Sample	Sintering temperature, °C	Bulk density ρ, g/cm^3	Porosity P, %	λ ($T = 25°$C), W·m^{-1}·K^{-1}
Compacted powder	–	2.242	55.3	–
1	1000	2.389	52.3	0.12±0.08
2	1100	2.767	44.8	0.42±0.08
3	1200	2.871	42.7	0.45±0.08
4	1300	3.627	27.6	1.35±0.08
5	1400	3.646	27.2	1.39±0.08

the activation of sintering and recrystallization processes lies in the temperature range of 1200–1300 °C. It should be noted that the obtained temperature range correlates well with the melting point value for the surface (nonautonomous) phase, calculated using the expression proposed in [50, 51].

Fig. 4 g,i shows the microstructure of samples 4 and 5 obtained at temperatures ≥1300 °C, which differs from samples 1, 2, and 3 by the absence of a fibrous structure. Due to a sharp increase in the contact area of grain boundaries and their recrystallization, pore formation occurs in the samples. In the image of the material obtained at 1300 °C (Fig. 4 h), the pore size varies in the range from 50 nm to several μm, which confirms active sintering of this material. An increase in the sintering temperature to up to 1400 °C leads to an increase in the pore size up to 3–5 μm (Fig. 4 j).

Table 1 presents the values of the total porosity and apparent density of the samples (powder and samples 1–5). As a result of dry uniaxial pressing of the powder at 4 MPa, the resulting material has a total porosity of $P = 55\%$ before the high-temperature treatment. Sintering at temperatures ≤1200 °C reduces the total porosity of the samples down to $P = 42\%$. The obtained values of the total porosity are consistent with the qualitative SEM data (Fig. 4 a–j) for samples 1–3, which show a large fraction of voids between the agglomerated $La_{0.9}Y_{0.1}PO_4$ monazite nanoparticles. As a result of an increase in the sintering temperature up to 1300 and 1400 °C (samples 4, 5), the material compactness increases to an apparent density of 3.65 g/cm^3, and the total porosity decreases down to $P \sim 27\%$.

Figure 5 shows the dependence of microhardness (H_v) at 25 °C on total porosity (P) of the samples (Table 1). A decrease in the total porosity of the material from 52% to 27%, which leads to an increase in H_v from 5±0.5 GPa to 17±0.5 GPa, shows that intense sintering and an increase in the hardness of porous materials based on a monazite structured $La_{0.9}Y_{0.1}PO_4$ solid solution occurs at temperatures ≥1300 °C. The obtained porous nanocrystalline materials have lower microhardness values than the known lanthanum orthophosphate-based monazite ceramics [46]. This is due to the difference in the microstructure and functional purpose of these materials. Large porosity and small microhardness values of the synthesized materials are due to the fact that this work was aimed at studying the possibility
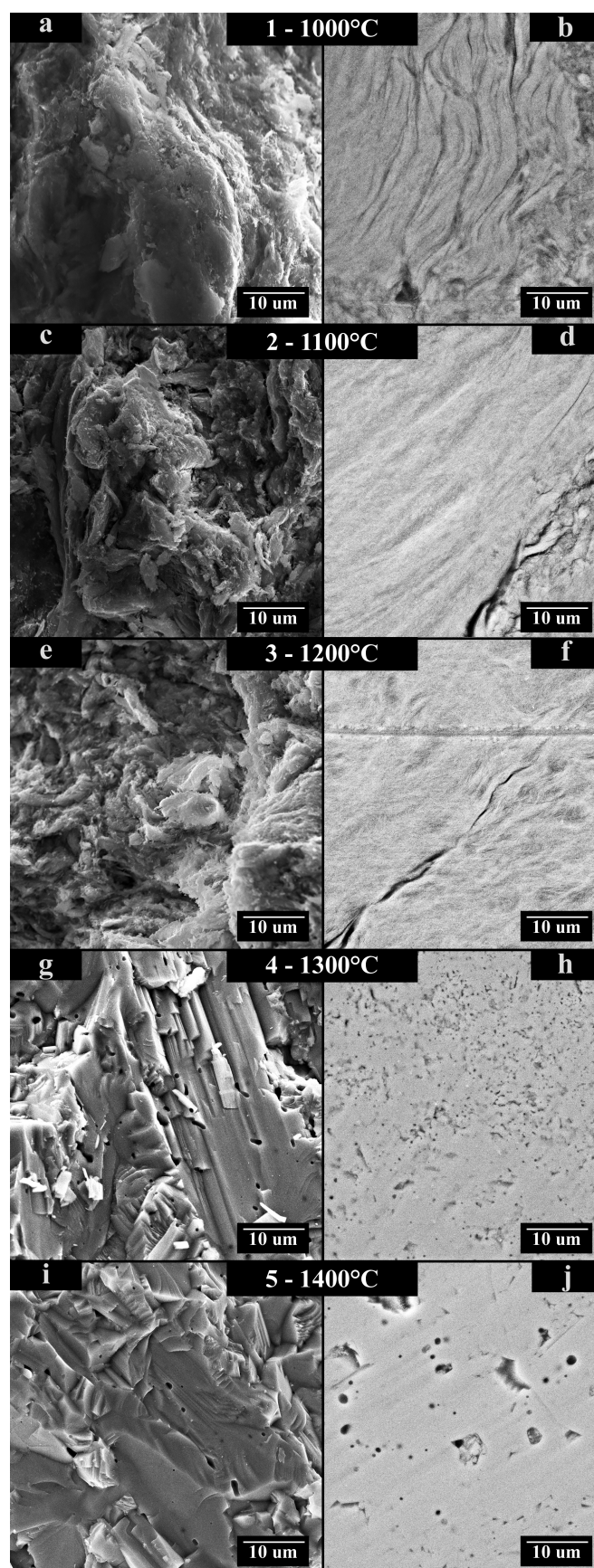
FIG. 4. SEM micrographs of samples heat treated at temperatures 1000 (1), 1100 (2), 1200 (3), 1300 (4) and 1400 °C (5): (a,c,e,g,i) splinters of cylindrical samples; (b,d,f,h,j) – polished sections of samples
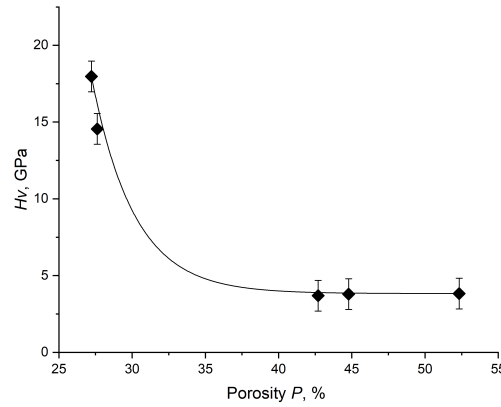
FIG. 5. Dependence of microhardness H_v on the total porosity P of the $La_{0.9}Y_{0.1}PO_4$-based materials
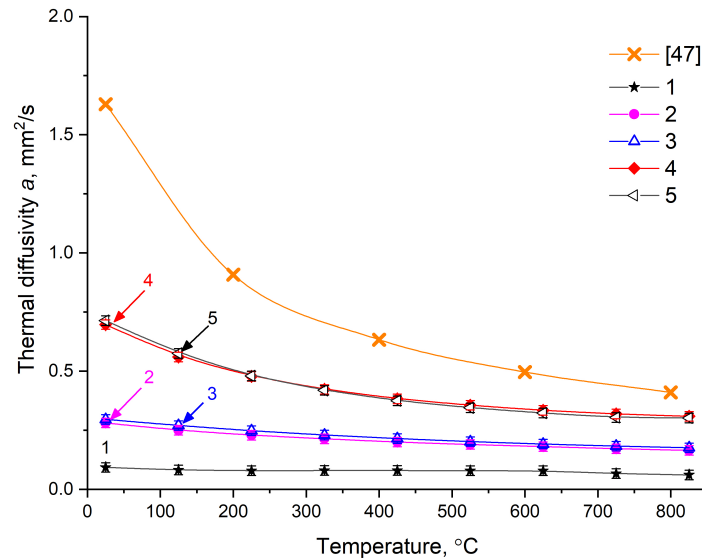

FIG. 6. Materials thermal diffusivity a after heat treatment at 1000 (1), 1100 (2), 1200 (3), 1300 (4), and 1400 °C (5)

of obtaining heat-insulating monazite structured *RE* phosphate-based materials, in contrast to the above works focused on obtaining non-porous ceramic materials for the radioactive waste form.

The dependence of thermal diffusivity (a) of materials (samples 1-5) on temperature ($T = 25 - 825$ °C) is shown in Fig. 6. For all the samples, a decrease in the a coefficient with the increasing temperature is inherent. The values of thermal diffusivity for samples 1–3 with total porosity of P=52–44% (Table 1) is lower than those for the samples with total porosity of $\approx$27% (samples 4, 5). The materials obtained at 1000–1200 °C displayed an almost linear character of the temperature diffusivity dependence on temperature; the values of a do not exceed 0.3 mm^2/s. As a result of material sintering and compaction, an increase in the thermal diffusivity occurs over the entire investigated temperature range. The obtained values depend on the total porosity and the size of the contact boundaries formed during the pressing of the powder. Fig. 6 shows that $a(T)$ values coincide within the error for samples 4 and 5 sintered at T =1300 °C and T =1400 °C, which is confirmed by their almost identical total porosity of $\sim$27%. The highest thermal diffusivity for the produced materials is 0.70$\pm$0.02 mm^2/s at T =25 °C for the samples obtained at 1300–1400 °C. The values of thermal diffusivity for the LaPO$_4$ monazite-based dense materials decrease monotonically from 1.629 mm^2/s (T=20 °C) down to 0.410 mm^2/s (T=800 °C) [47]. The minimum difference between the values of a obtained in the present study and those given in the literature is observed at high temperatures: a(800 °C)=0.410 mm^2/s ($P_{calc.}$=0%), and a(825 °C)=0.302$\pm$0.020 mm^2/s (sample 5, $P \sim$27%) in the present study.
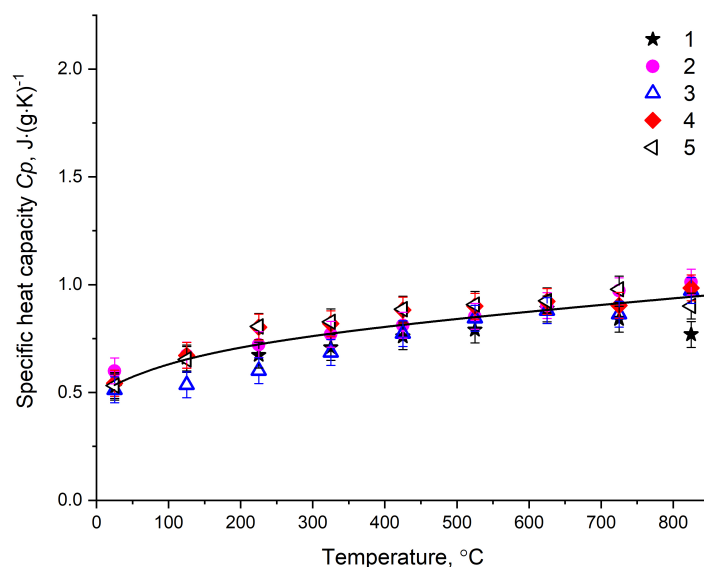
FIG. 7. Specific heat capacity (C_p) of the monazite structured La$_{0.9}$Y$_{0.1}$PO$_4$-based materials

Hence, it can be concluded that the thermal diffusivity, most likely, is less dependent on the total porosity of the monazite-based material.

The specific heat values of the sintered samples in Fig. 7 were calculated using the Mayer-Kelly empirical dependence equation ($C_p = a + bT + cT^{-2}$), the coefficients in which were determined from experimental data in the 25–825 °C range ($a = 0.66 \pm 0.06$, $b = (2.7 \pm 0.6) \cdot 10^{-4}$, $c = (-18.6 \pm 5.3) \cdot 10^3$). The specific heat values obtained for the monazite structured La$_{0.9}$Y$_{0.1}$PO$_4$-based material are higher than those for individual lanthanum orthophosphate with the same structure [30, 47, 48]. The character of $C_p(T)$ dependence is in good agreement with the authors' data for the monazite structured lanthanum orthophosphate, differing by 0.1–0.3 J·(g·K)$^{-1}$, which may be due to the presence of yttrium in the phase.

The values of thermal conductivity coefficient λ of samples 1-5 at $T = 25$ °C are presented in Table 1. The compaction of the La$_{0.9}$Y$_{0.1}$PO$_4$-based materials by increasing the processing temperature leads to an increase in the thermal conductivity from 0.12 ± 0.08 W·m^{-1}·K^{-1} at $P = 52.3\%$ up to 1.35 ± 0.08 W·m^{-1}·K^{-1} for samples 4 and 5 with a total porosity of $\approx 27\%$.

4. Conclusion

Pre-ceramic nanocrystalline powders have been obtained on the basis of a monazite structured La$_{0.9}$Y$_{0.1}$PO$_4$ solid solution. The powders are represented by quasi-one-dimensional particles with a crystallite size of about 16 nm. The nanoparticles were synthesized under hydrothermal conditions at 230 °C and a processing time of 110 minutes. The heat treatment of compacted nanocrystalline La$_{0.9}$Y$_{0.1}$PO$_4$ powder by the annealing-quenching method in the 1000–1400 °C range for 20 minutes resulted in polycrystalline compact materials with a total porosity of 27 to 52%. It is shown that the activation of nanopowder sintering and crystallite growth occurs in the 1200–1300 °C range, which correlates with the melting temperature of the surface (nonautonomous) phase.

The dependence of the thermophysical characteristics and microhardness of the material on the porosity has been determined. The maximum microhardness (H_v) value of 17 ± 0.5 GPa was obtained for the material with the lowest porosity. It was shown that the values of thermal diffusivity (a) of a material with total porosity (P) of 27% decreased monotonically with an increase in temperature from a ($T = 25$ °C)$= 0.70 \pm 0.02$ mm^2/s to a ($T = 825$ °C)$= 0.30 \pm 0.02$ mm^2/s. It was determined that the specific heat capacity of the monazite structured La$_{0.9}$Y$_{0.1}$PO$_4$-based material is higher than that of an individual lanthanum orthophosphate. The thermal conductivity of materials $\lambda(T = 25$ °C) varies depending on the porosity within a wide range from 0.12 ± 0.08 W·m^{-1}·K^{-1} at $P \approx 52\%$ to 1.35 ± 0.08 W·m^{-1}K^{-1} at $P \approx 27\%$.

Acknowledgement

The X-ray diffraction studies, determination of thermal diffusivity, examination by scanning electron microscopy, and the elemental analysis of samples were carried out on the instruments of the Engineering Center of the St. Petersburg State Technological Institute (Technical University).

The present work was financially supported by the Russian Foundation for Basic Research (Project No. 18-29-12119).

References

[1] Lomanova N.A., Tomkovich M.V., Danilovich D.P., Osipov A.V., Panchuk V.V., Semenov V.G., Pleshakov I.V., Volkov M.P., Gusarov V.V. Magnetic characteristics of nanocrystalline $BiFeO_3$-based materials prepared by solution combustion synthesis. *Inorg. Mater.*, 2020, **56**(12), P. 1271–1277.

[2] Martinson K.D., Kondrashkova I.S., Omarov S.O., D.A. Sladkovskiy D.A., Kiselev A.S., Kiseleva T.Yu., Popkov V.I. Magnetically recoverable catalyst based on porous nanocrystalline $HoFeO_3$ for processes of n-hexane conversion. *Advanced Powder Technology*, 2020, **31**(1), P. 402–408.

[3] Lomakin M.S., Proskurina O.V., Sergeev A.A., Buryanenko I.V., Semenov V.G., Voznesenskiy S.S., Gusarov V.V.Crystal structure and optical properties of the Bi–Fe–W–O pyrochlore phase synthesized via a hydrothermal method. *Journal of Alloys and Compounds*, 2021, **889**, P. 161598.

[4] Maslennikova T.P., Osipov A.V., Mezentseva L.P., Drozdova I.A., Kuchaeva S.K., Ugolkov V.L., Gusarov V.V. Synthesis, Mutual Solubility, and Thermal Behavior of Nanocrystals in the $LaPO_4$–YPO_4–H_2O System. *Glass Physics and Chemistry*, 2010, **36**(3), P. 351–357.

[5] Gavrichev K.S., Ryumin M.A., Tyurin A.V., Gurevich V.M., Komissarova L.N.. Refined heat capacity of $LaPO_4$ in the temperature range 0–1600K. Thermochimica Acta, 2008, **474**(1–2), P. 47–51.

[6] Clarke D.R., Phillpot S.R. Thermal barrier coating materials, *Materials Today*, 2005, **8**(6), P. 22–29.

[7] Chen D., Dambra C., Dorfman M. Process and properties of dense and porous vertically-cracked yttria stabilized zirconia thermal barrier coatings, *Surface and Coatings Technology*, 2020, **404**, P. 126467.

[8] Chen Y., Wang N., Ola O., Xia Y., Zhu Y. Porous ceramics: Light in weight but heavy in energy and environment technologies, *Materials Science and Engineering: R: Reports*, 2021, **143**, P. 100589.

[9] Mehboob G., Liu M.-J., Xu T., Hussain S., Mehboob G., Tahir A. A review on failure mechanism of thermal barrier coatings and strategies to extend their lifetime, *Ceramics International*, 2020, **46**(7), P. 8497–8521.

[10] Orlova A.I., Orlova V.A., Orlova M.P., Bykov D.M., Stefanovskii S.V., Stefanovskaya O.I., Nikonov B.S. The crystal-chemical principle in designing mineral-like phosphate ceramics for immobilization of radioactive waste. *Radiochemistry*, 2006, **48**, P. 330–339.

[11] Li M, Yuxian C., Lei G., Chenglong Z., Yuchen Z., Sixian H., Fuxing Y. Preparation of plasma sprayed nanostructured GdPO4 thermal barrier coating and its hot corrosion behavior in molten salts. *Ceram. Int.*, 2017, **43**(10), P. 7797–7803.

[12] Zhao Z., Heng C., Huimin X., Fu-Zhi D., Xiaohui W., Peng Z., Yanchun Z. $(La_{0.2}Ce_{0.2}Nd_{0.2}Sm_{0.2}Eu_{0.2})PO_4$: A high-entropy rare-earth phosphate monazite ceramic with low thermal conductivity and good compatibility with Al_2O_3. *J. Mater. Sci. Technol.*, 2019, **35**(12), P. 2892–2896.

[13] Monazite-based thermal barrier coatings: US6863999B1 USA F01D5/288, Sudre O.H., Marshall D.B., Morgan P.E.D. patent holder: Teledyne Scientific and Imaging LLC, 2005.

[14] Montel J.M., Glorieux B., Seydoux-Guillaume A.-M., Wirth R. Synthesis and sintering of a monazite–brabantite solid solution ceramic for nuclear waste storage. *J. Phys. Chem. Solids*, 2006, **67**(12), P. 2489–2500.

[15] Hikichi Y., Nomura T. Melting Temperatures of Monazite and Xenotime. *J. Am. Ceram. Soc*, 1987, **70**(10), P. 252–253.

[16] Galahov F.Y. Diagrammy sostoyaniya sistem tugoplavkih oksidov: spravochnik. V. 5. Dvojnye sistemy ch. 2. [State diagrams of refractory oxides]. Leningrad, Nauka, 1986, **5**, 359. (in Russian)

[17] Van Hoozen C.J., Gysi A.P., Harlov D.E. The solubility of monazite ($LaPO_4$, $PrPO_4$, $NdPO_4$, and $EuPO_4$) endmembers in aqueous solutions from 100 to 250°C. *Geochim. Cosmochim. Acta*, 2020, **280**, P. 302–316.

[18] Gratz R., Heinrich W. Monazite-xenotime thermobarometry; experimental calibration of the miscibility gap in the binary system $CePO_4$–YPO_4. *Am. Mineral.*, 1997, **82**(7), P. 772–780.

[19] Podor R., Cuney M., Nguyen T.C. Experimental study of the solid solution between monazite-(La) and $(Ca_{0.5}U_{0.5})PO_4$ at 780°C and 200 MPa. *Am. Mineral.*, 1995, **80**(11), P. 1261–1268.

[20] Huittinen N., Arinicheva Y., Kowalski P.M., Vinograd V.L., Neumeier S., Bosbach D. Probing structural homogeneity of $La_{1-x}Gd_xPO_4$ monazite-type solid solutions by combined spectroscopic and computational studies. *J. Nucl. Mater.*, 2017, **486**, P. 148–157.

[21] Zeng P., Teng Y., Huang Y., Wu L., Wang X. Synthesis, phase structure and microstructure of monazite-type $Ce_{1-x}Pr_xPO_4$ solid solutions for immobilization of minor actinide neptunium. *J. Nucl. Mater.*, 2014, **452**(1–3), P. 407–413.

[22] Arinicheva Y., Gausse C., Neumeier S., Brandt F., Rozov K., Szenknect S., Dacheux N., Bosbach D., Deissmann G. Influence of temperature on the dissolution kinetics of synthetic $LaPO_4$-monazite in acidic media between 50 and 130°C. *J. Nucl. Mater.*, 2018, **509**, P. 488–495.

[23] Ewing R.C., Wang L. Phosphates as nuclear waste forms. *Rev. Mineral.*, 2002, **48**(1), P. 673–699.

[24] Grechanovsky A.E., Eremin N.N., Urusov, V.S. Radiation resistance of $LaPO_4$ (monazite structure) and $YbPO_4$ (zircon structure) from data of computer simulation. *Phys. Solid State*, 2013, **55**(9), P. 1929–1935.

[25] Schlenz H., Heuser J., Neumann A., Schmitz S., Bosbach D. Monazite as a suitable actinide waste form. *Z. Kristallogr.*, 2013, **228**(3), P. 113–123.

[26] Yang Z., Yuan G., Duan X., Liang S., Sun G. HDEHP assisted solvothermal synthesis of monodispersed $REPO_4$ (RE = La–Lu, Y) nanocrystals and their photoluminescence properties. *New J. Chem.*, 2020, **44**(11), P. 4386–4393.

[27] Kenges K.M., Proskurina O.V., Danilovich D.P, Aldabergenov M.K., Gusarov V.V. Influence of the conditions for preparing $LaPO_4$-based materials with inclusions of the LaP_3O_9 phase on their thermal and mechanical properties. *Russ. J. Appl. Chem.*, 2018, **91**(9), P. 1538–1548.

[28] Thust A., Arinicheva Y., Haussühl E., Ruiz-Fuertes J., Bayarjargal L., Vogel S.C., Neumeier S., Winkler B. Physical properties of $La_{1-x}Eu_xPO_4$, $0 \leq x \leq 1$, monazite-type ceramics. *J. Am. Ceram. Soc.*, 2015, **98**(12), P. 4016–4021.

[29] Thust A., Hirsch A., Haussühl E., Schrodt N., Loison L., Schott P., Peters L., Roth G., Winkler B. Physical properties and microstructures of $La_{1-x}Pr_xPO_4$ monazite-ceramics. *Phys. Chem. Miner.*, 2018, **45**(4), P. 323–332.

[30] Min W., Daimon K., Matsubara T., Hikichi Y. Thermal and mechanical properties of sintered machinable $LaPO_4$–ZrO_2 composites. *Mater. Res. Bull.*, 2002, **37**(6), P. 1107–1115.

[31] Colomer M.T. Effect of Sr^{2+} doping on sintering behavior, microstructural development and electrical properties of $LaPO_4 \cdot nH_2O$ nanorods prepared by drymechanical milling. *Int. J. Hydrogen Energy*, 2018, **43**(29), P. 13462–13474.

[32] Arinicheva Y., Clavier N., Neumeier S., Podorb R., A.Bukaemskiy A., M.Klinkenberg M., Roth G., Dacheux N., Bosbach D. Effect of powder morphology on sintering kinetics, microstructure and mechanical properties of monazite ceramics. *J. Eur. Ceram. Soc.*, 2018, **38**(1), P. 227–234.

[33] Proskurina O.V., Sivtsov E.V., Enikeeva M.O., Sirotkin A.A., Abiev R. Sh., Gusarov V.V. Formation of rhabdophane-structured lanthanum orthophosphate nanoparticles in an impinging-jets microreactor and rheological properties of sols based on them. *Nanosyst. Physics, Chem. Math*, 2019, **10**(2), P. 206–214.

[34] Li P., Zhang Y., Zhang L., Li F., Guo Y., Li Y., Gao W. Phase control of Eu^{3+}-doped YPO_4 nano-/microcrystals. *Cryst. Growth Des.*, 2017, **17**(11), P. 5935–5944.

[35] Ugolkov V.L., Mezentseva L.P., Osipov A.V., Popova V.F., Maslennikova T.P., Akatov A.A., Doil'nitsyn V.A. Synthesis of Nanopowders and Physicochemical Properties of Ceramic Matrices of the $LaPO_4$–YPO_4–(H_2O) and $LaPO_4$–$HoPO_4$–(H_2O) Systems. *Russian Journal of Applied Chemistry*, 2017, **90**(1), P. 28–33.

[36] Terra O., Clavier N., Dacheux N., Podorb R. Preparation and characterization of lanthanum–gadolinium monazites as ceramics for radioactive waste storage. *New J. Chem.*, 2003, **27**(6), P. 957–967.

[37] Deschanels X., Seydoux-Guillaume A.M., Magnin V., Mesbah A., Tribet M., Moloney M.P., Serruys Y., Peuget S., Swelling induced by alpha decay in monazite and zirconolite ceramics: A XRD and TEM comparative study. *J. Nucl. Mater.*, 2014, **448**(1–3), P. 184–194.

[38] Martel L., Islam Md. A., Popa K., Vigier J.-F., Colineau E., Bolvin H., Griveau J.-C. Local structure and magnetism of $La_{1-x}M_xPO_4$ (M=Sm, ^{239}Pu, ^{241}Am) explained by experimental and computational analyses. *J. Phys. Chem.*, 2021, **125**(40), P. 22163–22174.

[39] Morgan P.E.D., Marshall D.B. Ceramic composites of monazite and alumina. *J. Am. Ceram.*, 1995, **78**, P. 1553–1563.

[40] Wu J., Jia H., Li M., Liu Z. Influence of pH on nano-phosphor YPO_4:2%Sm^{3+} and luminescent properties. *Appl. Phys. A*, 2020, **126**(2), P. 87.

[41] Enikeeva M.O., Kenges K.M., Proskurina O.V., Danilovich D.P., Gusarov V.V. Influence of hydrothermal treatment conditions on the formation of lanthanum orthophosphate nanoparticles of monazite structure. *Russ. J. Appl. Chem.*, 2020, **93**(4), P. 540–548.

[42] Fan W., Song X., Bu Y., Sun S., Zhao X. Selected-control hydrothermal synthesis and formation mechanism of monazite- and zircon-type $LaVO_4$ nanocrystals. *J. Phys. Chem. B*, 2006, **110**(46), P. 23247–23254.

[43] Bryukhanova K.I., Nikiforova G.E., Gavrichev K.S. Synthesis and study of anhydrous lanthanide orthophosphate (Ln = La, Pr, Nd, Sm) nanowhiskers. *Nanosyst. Physics, Chem. Math*, 2016, **7**(3), P. 451–458.

[44] Rafiuddin M.R., Grosvenor A.P. A structural investigation of hydrous and anhydrous rare-earth phosphates. *Inorg. Chem.*, 2016, **55**(19), P. 9685–9695.

[45] Hirsch A., Kegler P., Alencar I., Ruiz-Fuertes J., Shelyug A., Peters L., Schreinemachers C., Neumann A., Neumeier S., Liermann H., Navrotsky A., Roth G. Structural, vibrational, and thermochemical properties of the monazite-type solid solution $La_{1-x}Pr_xPO_4$. *J. Solid State Chem.*, 2017, **245**, P. 82–88.

[46] Perri Ere L., Bregiroux D., Naitali B., Audubert F., Champion E., Smith D.S., Bernache-Assollant D. Microstructural dependence of the thermal and mechanical properties of monazite $LnPO_4$ (Ln= La to Gd). *J. Eur. Ceram. Soc.*, 2007, **27**(10), P. 3207–3213.

[47] Du A., Wan C., Qu Z., Pan W. Thermal Conductivity of Monazite-Type $REPO_4$ (RE=La, Ce, Nd, Sm, Eu, Gd). *J. Am. Ceram. Soc.*, 2009, **92**(11), P. 2687–2692.

[48] Du A., Wan C., Qu Z., Pan W. Effects of texture on the thermal conductivity of the $LaPO_4$ Monazite. *J. Am. Ceram. Soc.*, 2010, **93**(9), P. 2822–2827.

[49] Maier C.G., Kelley K.K. An equation for the representation of high-temperature heat content data. *J. Am. Chem. Soc.*, 1932, **54**(8), P. 3243–3246.

[50] Gusarov V.V., Suvorov S.A. Melting points of locally equilibrium surface phases in polycrystalline systems based on a single volume phase. *J. Appl. Chem. of the USSR*, 1990, **63**(8), P. 1560–1565.

[51] Gusarov V.V. The thermal effect of melting in polycrystalline systems. *Thermochim. Acta*, 1995, **256**(2), P. 467–472.